Applied Catalysis B: Environmental 343 (2024) 123545

Contents lists available at ScienceDirect

Applied Catalysis B: Environmental

journal homepage: www.elsevier.com/locate/apcatb

Built-in electric field mediated S-scheme charge migration in COF/In_2S_3 heterojunction for boosting H_2O_2 photosynthesis and sterilization

Hanye Chen [a], Shengjie Gao [a], Guocheng Huang [a,*], Qiaoshan Chen [a], Yanxin Gao [a], Jinhong Bi [a,b,**]

[a] Department of Environmental and Safety Engineering, Fuzhou University, Minhou, Fujian 350108, China
[b] State Key Laboratory of Photocatalysis on Energy and Environment, Fuzhou University, Minhou, Fujian 350108, China

ARTICLE INFO

Keywords:
H_2O_2 production
Covalent organic frameworks
S-scheme heterojunction
Built-in Electric Field
In situ XPS

ABSTRACT

The construction of step-scheme (S-scheme) heterojunctions has emerged as a widely adopted strategy for achieving photocatalytic hydrogen peroxide (H_2O_2) generation. In this study, we employed an approach to deposit indium sulfide (In_2S_3) onto a Schiff-base covalent organic framework (COF), namely TpMA, for H_2O_2 photosynthesis and its sterilization application. The optimized photocatalyst, 10%TpMA/In_2S_3, exhibited remarkable photocatalytic performance, yielding a substantial H_2O_2 output of 311.07 μmol/L. A series of advanced instrumental analyses and density functional theory (DFT) results indicated that the establishment of the S-scheme heterojunction played a pivotal role in facilitating efficient charge carrier transfer and separation. Specifically, the formation of a built-in electric field was probed and quantified. Furthermore, the H_2O_2 exhibited the capability to undergo direct catalysis by Fe(II), which substantially facilitated the inactivation of pathogenic bacteria. This work unveils insight into the COF-based S-scheme photocatalysts and offers a sustainable approach for environmentally friendly H_2O_2 production for sterilization purposes.

1. Introduction

Hydrogen peroxide (H_2O_2) stands as a versatile and environmentally benign substance with wide-ranging applications in environmental protection, notably in water treatment and disinfection [1–3]. However, the conventional anthraquinone (AQ) method for H_2O_2 production has been associated with safety concerns due to the explosive nature of H_2/O_2 mixtures [4,5]. Consequently, there has been a growing interest in exploring alternative, safe, and environmentally sustainable approaches for H_2O_2 synthesis [6].

Semiconductor photocatalysis, leveraging harmless materials (H_2O and O_2) and utilizing sunlight as an energy source, has garnered considerable attention as a promising avenue for H_2O_2 production. This method involves the generation of H_2O_2 through the two-electron reduction of dissolved oxygen in water, facilitated by the photogenerated electrons of the semiconductor photocatalyst [7]. This approach is not only cost-effective but also environmentally friendly, safe, and dependable. Nevertheless, conventional semiconductor photocatalysts have their limitations. For instance, titanium dioxide (TiO_2) can only be activated by ultraviolet light, restricting its utilization under sunlight [8]. Moreover, traditional methods often require noble metal co-catalysts, leading to suboptimal photocatalytic efficiencies [9,10]. Consequently, recent research efforts have focused on organic-based semiconductor materials such as covalent organic frameworks (COFs) [11], metal-organic frameworks (MOFs) [12], and graphite phase carbon nitride [13], which have exhibited promising potential. For example, Qin et al. [14] synthesized ultrathin nanocrystalline g-C_3N_4 (NS-g-C_3N_4) by a simple one-step calcination method. The efficiency and selectivity of photocatalytic reduction of CO_2 to CO were higher than that of bulk phase (B-g-C_3N_4) under visible light. Lai et al. [15] first synthesized $BiOIO_3$ (CQDs/$BiOIO_3$) loaded with carbon quantum dots. 3 wt% CQDs/$BiOIO_3$ had the highest photodegradation efficiency of bisphenol A (95.01%) after 60 min. Among these materials, COFs are characterized by their controlled and periodic structure with columnar stacking of nanosheets and offer an organized electron channel system [16], which is advantageous to carrier transport in the stacking direction [17]. However, typical single semiconductor photocatalysts suffer from limitations such as limited visible light absorption, rapid electron-hole

* Corresponding author.
** Corresponding author at: Department of Environmental and Safety Engineering, Fuzhou University, Minhou, Fujian 350108, China.
E-mail addresses: sysuhgc@gmail.com, huanggch@fzu.edu.cn (G. Huang), bijinhong@fzu.edu.cn (J. Bi).

https://doi.org/10.1016/j.apcatb.2023.123545
Received 3 October 2023; Received in revised form 9 November 2023; Accepted 19 November 2023
Available online 21 November 2023
0926-3373/© 2023 Elsevier B.V. All rights reserved.

recombination, and sluggish reaction kinetics. Therefore, selecting appropriate carriers to design and manufacture semiconductor heterojunction materials to overcome these issues remains a challenge.

To enhance the photocatalytic efficiency of COFs, various strategies, including surface modification [18], noble metal doping [19], and heterojunction fabrication [20], have been explored. For instance, bimetallic PdIn nanoclusters were combined with a sensitive COF (N_3-COF), resulting in robust photoreduction activity for CO_2 [21]. Similarly, COFs based on thiophene-porphyrin have exhibited improved CO evolution rates through heterojunction formation [22]. Among these strategies, heterojunction creation has shown particular promise in enhancing photocatalyst performance [23]. For instance, the combination of g-C_3N_4 and Tp-Tta COF led to a novel van der Waals heterojunction, substantially improving photocatalytic CO_2 reduction [24]. Additionally, a direct Z-scheme heterostructure between COF and metal sulfide was created, significantly enhancing H_2O reduction properties [25]. Furthermore, an all-solid-state Z-scheme g-C_3N_4/m-Bi_2O_4 heterojunction effectively inactivated pathogenic bacteria under visible light irradiation [26]. Under visible light irradiation, 6 $\log_{10}$ cfu/mL of *E. coli* K-12 could be totally inactivated in 1.5 h; however, under the same experimental conditions, pure g-C_3N_4 and Bi_2O_4 had activities of 1.2 $\log_{10}$ cfu/mL and 3.2 $\log_{10}$ cfu/mL, respectively. Nevertheless, the mechanisms governing charge transfer in Z-scheme heterojunctions remain contentious, prompting exploration of alternative theories. Recently, Yu et al. [27] proposed a novel concept of S-scheme heterojunction, in which the photocatalysts simultaneously generate electron-hole pairs via the parallel connection of two distinct semiconductor materials An example could be came from Xu et al. [28], who synthesized TiO_2/$CsPbBr_3$ composite S-scheme heterojunction by self-assembly. DFT calculations and *in situ* X-ray photoelectron spectroscopy (*in situ* XPS) showed that the combination of the two can induce the transfer of electrons from $CsPbBr_3$ quantum dots to TiO_2, and then resulted in the formation of an internal electric field (IEF), which promoted the separation of photogenerated charge and boosted photocatalytic reduction ability of CO_2. Despite these novel insights, selecting appropriate counterparts to construct the COF-based S-scheme photocatalysts is still a challenging task.

In_2S_3, characterized by its ordered structure, exceptional electrochemical properties, and high stability, represents a promising n-type semiconductor photocatalyst candidate with a narrow band gap [29]. Heterojunctions involving In_2S_3 have been shown to enhance electron conduction, resulting in remarkable photocatalytic activity under visible light irradiation. For example, Zhang et al. [30] fabricated a heterojunction based on In_2S_3 to speed up electron conduction in the system, and the optimal photocatalyst produced 902.9 μmol H_2O_2 through 5 h visible light irradiation. Qiu et al. [31] demonstrated that the In_2S_3 photocatalyst had a significant inactivation effect on *E. coli* under fluorescence tube irradiation. The band structure of TpMA and In_2S_3 shows the feasibility of forming the S-scheme heterojunction between TpMA and In_2S_3. However, advanced oxidation processes (AOPs), rather than traditional disinfection techniques, are becoming more and more popular for the inactivation of germs. One of the most extensively used and viable AOPs is the photocatalysis-Fenton technique. Because traditional Fenton reagents necessitate the addition of oxidants (e.g., H_2O_2), higher operating expenses are unavoidable [32]. It would be interesting to conduct study on delivering the oxidant needed by the Fenton process using the H_2O_2 produced by the photocatalytic process.

Herein, we report an S-scheme heterojunction formed by In_2S_3 and TpMA nanotubes, and their activity of H_2O_2 production and bacterial inactivation was compared with pristine TpMA. The morphology, crystal structure, and photochemical properties of TpMA/In_2S_3 photocatalyst were analyzed integrally. In addition, without adding H_2O_2, the photocatalysis-Fenton system was designed for bacteria inactivation by combining in situ generated H_2O_2 with Fe(II). The development of cleaner and sustainable production pathways through the design and construction of the TpMA/In_2S_3 S-scheme heterojunction offers fresh insights into COFs-based photocatalysts for H_2O_2 generation.

2. Experimental

Pristine TpMA was prepared by the solvothermal method. As shown in Fig. 1a, 1,3,5-Triformylphloroglucinol (Tp, 0.5 mmol, 0.105 mg) and melamine (MA, 0.5 mmol, 0.063 mg) were dissolved in a high-temperature and pressure-resistant glass bottle filled with a ternary solvent mixture of mesitylene/1,4-dioxane/3 M acetic acid (5/5/1 by vol.; 11.0 mL). The reaction mixture was sonicated fully, bubbled with N_2 for 15 min, and then heated at 120 °C for 3 d. After the mixture cooled to room temperature, the precipitate was isolated by centrifugation while being washed with acetone, tetrahydrofuran (THF), and 80 °C water. The obtained powder was dried under vacuum at 120 °C for 10 h.

TpMA/In_2S_3 hybrids with different In_2S_3 loading amounts were synthesized by a hydrothermal method. Typically, to synthesize 10 wt% TpMA/In_2S_3 (10%TpMA/In_2S_3), a stoichiometric ratio of $In_2(SO_4)_3$•6 H_2O (1.0 mmol) and thioacetamide (3.6 mmol) and fixed quality TpMA (0.1 mmol) was dissolved in 60 mL ultrapure water, the reaction liquid was sonicated for 20 min so that the precursor fully precipitates on TpMA. The mixes were then put into a 100 mL Teflon-lined autoclave and heated to 160 °C for 12 h after being violently agitated for 1 h. Following the reaction period and cooling to room temperature, the product underwent repeated washes with ethanol and ultrapure water before being dried in a vacuum for 10 h at 80 °C. Other proportional products were synthesized by changing simply the quality of the precursor. TpMA was not added in the synthesis of pure In_2S_3. The detailed information of materials, characterizations, photoelectrochemical measurements and theoretical calculations were illustrated in the Supporting Information.

3. Results and discussion

3.1. Structure and morphology analyses of TpMA/In_2S_3

The structural and morphological characteristics of TpMA/In_2S_3 were comprehensively examined through various analytical techniques. X-ray diffraction (XRD) patterns of TpMA, In_2S_3, and TpMA/In_2S_3 are depicted in Fig. 1b. Several prominent peaks were observed in the 2 theta range from 3° to 35°, with In_2S_3 being indexed to a hexagonal crystal structure and the diffraction peaks of TpMA indicated a framework with a specific structural order (JCPDS 65–0459) [29]. With increasing proportions of TpMA, a slight reduction in the intensity of the peak around 30° was noted, attributable to the relatively weak crystallization of TpMA. This effect suggests that inadequate In_2S_3 coverage on the TpMA surface gradually leads to surface exposure [33]. Notably, no discernible shift in peak positions or emergence of new peaks was observed, underscoring the preservation of original lattice structures within the TpMA/In_2S_3 samples [34].

Fourier transform infrared (FT-IR) spectra of TpMA, In_2S_3 and TpMA/In_2S_3 samples, as illustrated in Fig. 1c, displayed characteristic peaks similar to those of the parent TpMA. Specifically, the peaks at around 1508 cm^{-1} and 1380 cm^{-1} corresponded to the typical stretching mode and breathing mode of aromatic C-N in the triazine rings [35, 36], indicating that TpMA was maintained after the formation of heterojunction. Additionally, the TpMA/In_2S_3 samples exhibited an infrared absorption peak at 1609 cm^{-1}, signifying the presence of C═O groups. This suggested that the success of an irreversible enol-keto tautomerization reaction, which was anticipated to effectively improve the stability of TpMA [37].

Morphological assessments of TpMA and TpMA/In_2S_3 were conducted using transmission electron microscopy (TEM) and scanning electron microscopy (SEM), as depicted in Fig. 1d-f. In_2S_3 exhibited a flake cluster morphology (Fig. S1a), whereas pristine TpMA nanotubes displayed lengths on the order of several microns. In comparison to the

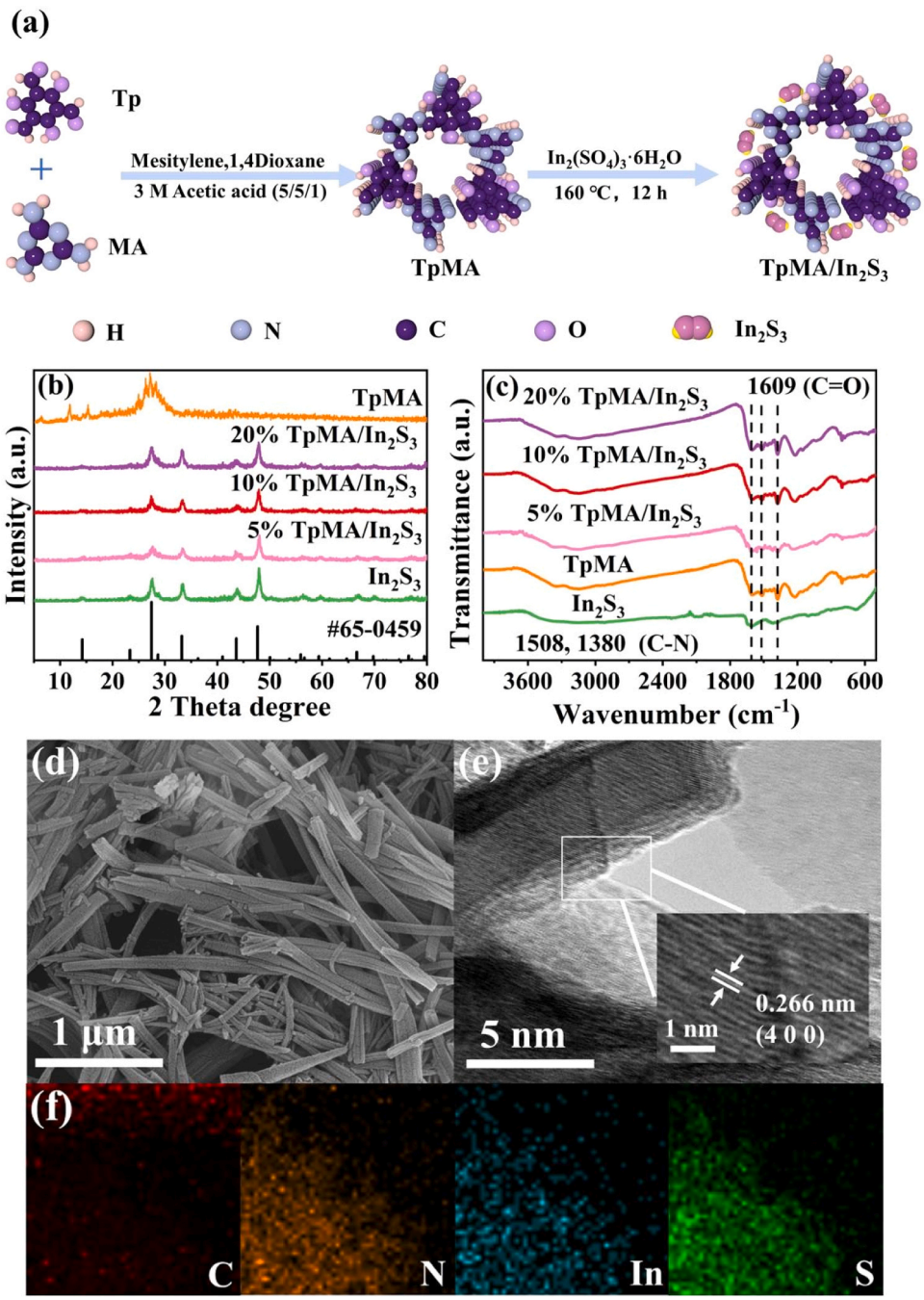

Fig. 1. Schematic illustration of the synthesis process for TpMA/In_2S_3 (a), XRD (b), and FT-IR (c) patterns of TpMA, In_2S_3 and TpMA/In_2S_3 samples. SEM image of TpMA (d), TEM image of TpMA/In_2S_3 (e), EDX elemental mapping of TpMA/In_2S_3 sample (f).

SEM image of TpMA (Fig. 1d), TpMA/In_2S_3 (Fig. S1b) revealed the stacking of In_2S_3 sheets atop TpMA nanotubes. Fig. 1e demonstrates the stacking of the TpMA nanotubes and the presence of lattice fringes on their surfaces, which have a spacing of 0.266 nm consistent with the In_2S_3 crystal plane (400). The energy-dispersive X-ray (EDX) elemental mapping based on TpMA/In_2S_3 (Fig. 1f) shows the distribution of four elements (C, N, In, and S) across the map layer, and particularly, the In and S mapping further substantiating the binding of In_2S_3 to the surface of TpMA nanotubes. The Brunauer-Emmett-Teller (BET) surface area (S_{BET}) and pore size distribution were measured to investigate the variation of porous structure and specific surface area of the sample subjected to modification. The adsorption-desorption isothermal curves of TpMA and 10%TpMA/In_2S_3 samples (Fig. S2) corresponded to type IV pattern, and the hysteresis rings of the isothermal curves within the relative pressure range of 0.45–1.0 belonged to type H3, indicating the presence of stacked porous structures in all samples. Notably, 10% TpMA/In_2S_3 exhibited an improved average pore volume compared to TpMA, signifying enhanced molecular adsorption capacity. Specifically, as presented in Table S1, 10%TpMA/In_2S_3 displayed a smaller S_{BET} and Vpore of 82.41 m^2/g and 0.25 cm^3/g, respectively, in contrast to TpMA (105.94 m^2/g and 0.3730 cm^3/g). It underscored the effective accommodation of In_2S_3 within the mesoporous structure of TpMA. This observation aligns with the SEM and TEM characterizations, validating the structural attributes of the composite material.

3.2. Analysis of band structures in TpMA/In_2S_3

The optical characteristics of TpMA, In_2S_3, and TpMA/In_2S_3 were

thoroughly investigated utilizing UV-vis diffuse reflectance spectra (UV-vis DRS), as presented in Fig. 2a. Both TpMA and In_2S_3 exhibited typical absorption patterns indicative of semiconductors, allowing for the determination of their respective band gap energies (E_g). TpMA exhibited an E_g of 2.36 V, while In_2S_3 displayed an E_g of 1.97 V. Remarkably, the optical absorption properties of TpMA/In_2S_3 were significantly enhanced across the entire tested wavelength range, accompanied by a redshift in the absorption edge. This phenomenon signifies that the formation of the heterojunction could enhance light absorption properties, broadening the absorption edge and thereby enabling the activation of a greater number of photogenerated charge carriers essential for the photocatalytic process. To further elucidate the band structure of TpMA and In_2S_3, the Mott-Schottky plots (Figure. S3) of TpMA and In_2S_3 samples employed to determine the relative positions of conduction band (CB) potentials. The flat-band potentials were estimated to be - 0.42 V and - 0.78 V (vs. NHE) for TpMA and In_2S_3, respectively. Subsequently, the electronic band structure diagrams for TpMA and In_2S_3 could be obtained based on the aforementioned UV-vis DRS spectra and Mott-Schottky plot results (Fig. 2b). Specifically, the valence band (VB) potentials of TpMA and In_2S_3 were determined to be 1.94 V and 1.19 V, respectively, and are compatible with earlier studies [33,37]. Consequently, the band structures of the tailored heterojunctions satisfy the feasibility to construct an S-scheme junction, in which a staggered band structure is an essential prerequisite.

3.3. Photoelectrochemical properties of TpMA/In_2S_3

Electrochemical impedance spectroscopy (EIS) plots disclosed the charge transfer kinetics of the photocatalysts at the electrode interface [38]. As shown in Fig. 2c, 10%TpMA/In_2S_3 had the smallest impedance, indicative of its superior electron transport capability. The observation demonstrated that 10%TpMA/In_2S_3 had a significantly increased charge separation efficiency, allowing for a greater number of electrons and holes to participate in the photocatalytic reaction and presumably indicative of better H_2O_2 yield over the composites than the pristine samples[39]. Meanwhile, Transient photocurrent responses, representing the photocatalytic activity of electrons, were measured for TpMA, In_2S_3 and 10%TpMA/In_2S_3 samples with multiple on-off cycles, as displayed in Fig. 2d. Likewise, the observed photocurrent intensities varied among the materials and the 10%TpMA/In_2S_3 samples exhibited the greatest photocurrent density.

Photoluminescence (PL) spectroscopy was conducted on TpMA and 10%TpMA/In_2S_3 samples upon excitation at 400 nm. As illustrated in Fig. S4, both TpMA and 10%TpMA/In_2S_3 exhibited broad fluorescence emission peaks in the visible region. Notably, 10%TpMA/In_2S_3 demonstrated pronounced fluorescence quenching relative to TpMA, resulting in lower PL intensity. This phenomenon signified the enhanced light carrier separation rate and reduced recombination rate in 10% TpMA/In_2S_3, contributing to the improved rate of photocatalytic H_2O_2 production [40].

3.4. Photocatalytic activity of TpMA/In_2S_3

The photocatalytic performance of the samples was assessed in pure water under visible light irradiation. As depicted in Fig. 2e, the pristine TpMA and pure In_2S_3 showed limited activity, generating about 237.14 μmol/L and 31.76 μmol/L H_2O_2 within 90 min, respectively. Notably, the x%TpMA/In_2S_3 samples exhibited remarkably higher activity than pristine TpMA and pure In_2S_3. Among these, 10%TpMA/In_2S_3 showed the highest activity, yielding 311.07 μmol/L. To further investigate the recyclability of 10%TpMA/In_2S_3, the photocatalytic H_2O_2 production experiment was repeated for a total of four cycles (Fig. S5). Notably, the 10%TpMA/In_2S_3 consistently demonstrated a high level of photocatalytic activity for H_2O_2 production throughout the four consecutive experimental runs, substantiating its inherent robustness and stability. A slight decline of H_2O_2 yield to 302.23 μmol/L was observed in the last run, which could be attributed to the loss of catalyst in the washing process. Furthermore, the XRD patterns and FT-IR plots of recycled and original 10%TpMA/In_2S_3 are compared in Fig. S6. The crystalline structure of the 10%TpMA/In_2S_3 remained intact after successive cycles

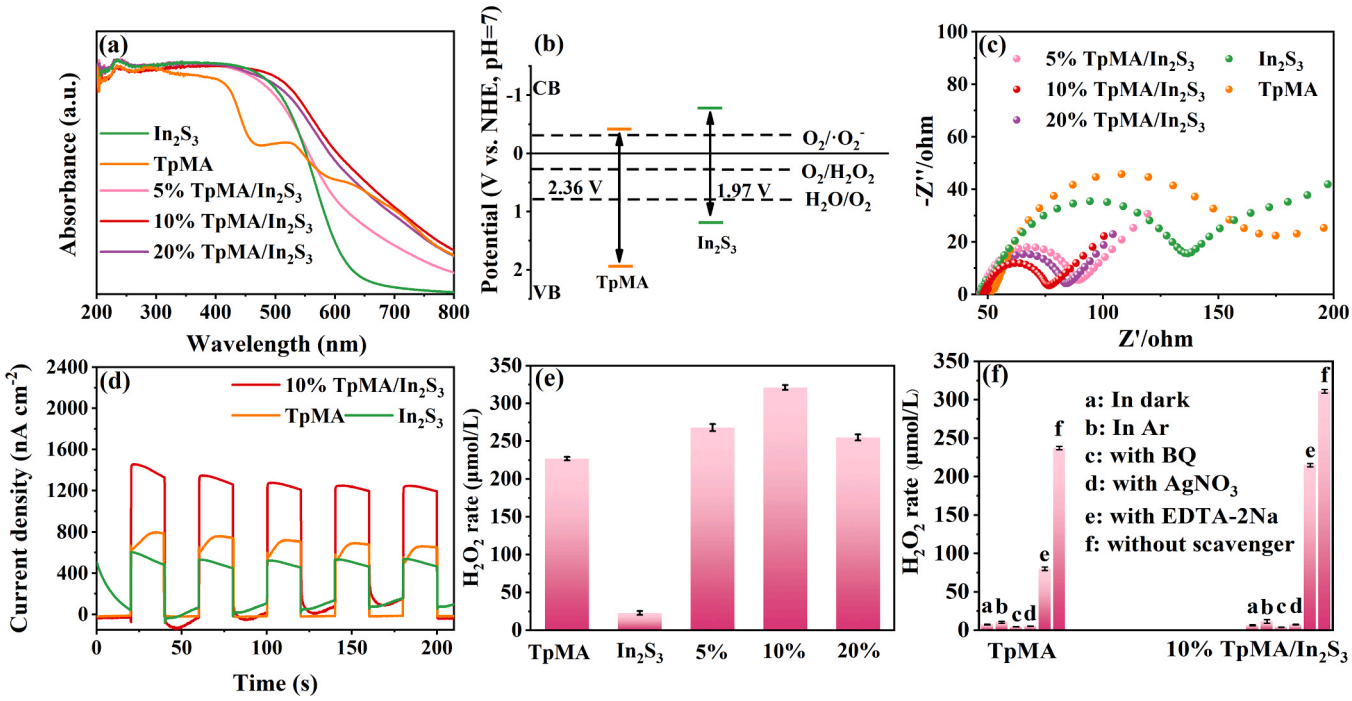

Fig. 2. DRS of TpMA, In_2S_3 and TpMA/In_2S_3 samples (a), schematic illustration of band structures of TpMA and In_2S_3 samples (b), electrochemical impedance spectroscopy plots (c), periodic on/off photocurrent response under visible light irradiation for TpMA and TpMA/In_2S_3 samples (d), production of H_2O_2 on prepared photocatalysts under light irradiation (e), the influence of different condition and various scavengers on the H_2O_2 production ability over as-prepared catalysts (f). Error bars represent standard deviations (n = 3).

of the photocatalytic reaction, signifying its potential for recyclability.

3.5. Mechanism of H_2O_2 photosynthesis

As shown in Fig. 2f, the influence of different conditions and various scavengers on the H_2O_2 production ability over TpMA and 10%TpMA/In_2S_3 were explored. Both of TpMA and 10%TpMA/In_2S_3 showed reduced activity in dark or within an Argon atmosphere highlighting that O_2 is an important essential component in the photocatalytic generation of H_2O_2. Furthermore, the introduction of para-benzoquinone (BQ) and $AgNO_3$ (1 mmol/L) as scavenger to capture $\cdot O_2^-$ and electron revealed that $\cdot O_2^-$ was an indispensable participant in the reaction process. Unsurprisingly, the reduction of oxygen by electrons played a vital role. The addition of the hole-trapping agent ethylenediaminetetraacetic acid disodium salt (EDTA-2Na) only partially affected the reaction activity, indicating that the catalyst not only utilizes holes for oxygen production but also exploits dissolved oxygen in water for H_2O_2 generation during the reaction. This hypothesis was verified by the presence of dissolved oxygen in a sealed reactor during the reaction period (Fig. S7). The yield of dissolved oxygen was consistent with that of hydrogen peroxide, suggesting that the 10%TpMA/In_2S_3 samples could proceed water oxidation to produce O_2, which in turn could be a source of O_2 to facilitate subsequent reactions of H_2O_2 production.

Insight into the photocatalytic H_2O_2 generation process over 10% TpMA/In_2S_3 was further probed by *in situ* Fourier transform spectra (*in situ* FT-IR). As shown in Fig. 3a and b, the intensities of O-O bonding at 940 cm^{-1} and the$\cdot O_2^-$ at 1163 cm^{-1} underwent marked enhancement with the increasing irradiation time, confirming the formation of $\cdot O_2^-$ and the mechanism of two-step single-electron pathway. Ultraviolet photoelectron spectroscopy (UPS) analysis was employed to calculate the work function (Φ) and Fermi level (E_{Fermi}) of the samples. As shown in Fig. S8, the Φ of In_2S_3, TpMA and 10%TpMA/In_2S_3 were calculated to be 4.22 eV, 5.02 eV, and 4.83 eV. The Fermi level of In_2S_3, TpMA and 10% TpMA/In_2S_3 are -0.28 eV, 0.52 eV, and 0.33 eV, respectively. It is therefore could be inferred that band bending occurred between TpMA and In_2S_3, and a built-in electric field was established between TpMA and In_2S_3, which is the essential prerequisite for forming S-scheme heterojunction.

Typically, IEF is generally regarded as the driving force for a fast charge transfer at the S-scheme interface. The IEF magnitude of the TpMA, In_2S_3 and 10%TpMA/In_2S_3 was calculated by using the following equation (Eq. 1) developed by Kanata et al. [41].

$$Fs = \left(\frac{-2V_s\rho}{\varepsilon\varepsilon_0}\right)^{1/2} \quad (1)$$

Where Fs is the internal electric field magnitude, V_s is the surface voltage, ρ is the surface charge density, ε is the low-frequency dielectric constant, and ε_0 is the permittivity of free space. The above equation reveals that the internal electric field magnitude is mainly determined by the surface voltage and the charge density because ε and ε_0 are two constants. As shown in Fig. 3c and d, all the samples exhibited positive surface photovoltage (SPV) signals, indicating that the material has the characteristics of n-type semiconductor. Notably, 10%TpMA/In_2S_3 exhibited the strongest SPV signal, signifying its capacity to generate more photogenerated carriers under light. Fig. 3e showed the transient photocurrent curve. Based on the finding by Chen et al. [42], the integration of the recorded transient photocurrent density minus the steady-state photocurrent relative to time can yield a value proportional to the number of positive charges deposited on the surface. The charge density value of TpMA, In_2S_3 and 10%TpMA/In_2S_3 were accordingly determined as 1.63 μC/cm^2, 1.28 μC/cm^2 and 2.22 μC/cm^2. The strengths of the calculated internal electric field were normalized by setting the built-in electric field strength of In_2S_3 to "1". The calculated electric field strength of TpMA was "38.9", which was stronger than In_2S_3. 10%TpMA/In_2S_3 has the highest built-in electric field intensity of "51.2", which was significantly higher than that of the two counterpart materials and these results were consistent with the results from the activity tests. The strong internal electric field facilitates rapid separation of photogenerated carriers, a key factor contributing to the enhanced H_2O_2 photosynthesis. These findings align well with the theory of S-scheme heterojunction and substantiate the increase in H_2O_2 production.

The electron paramagnetic resonance (EPR) was applied to identify the reactive oxygen species generated by the reaction of TpMA, In_2S_3

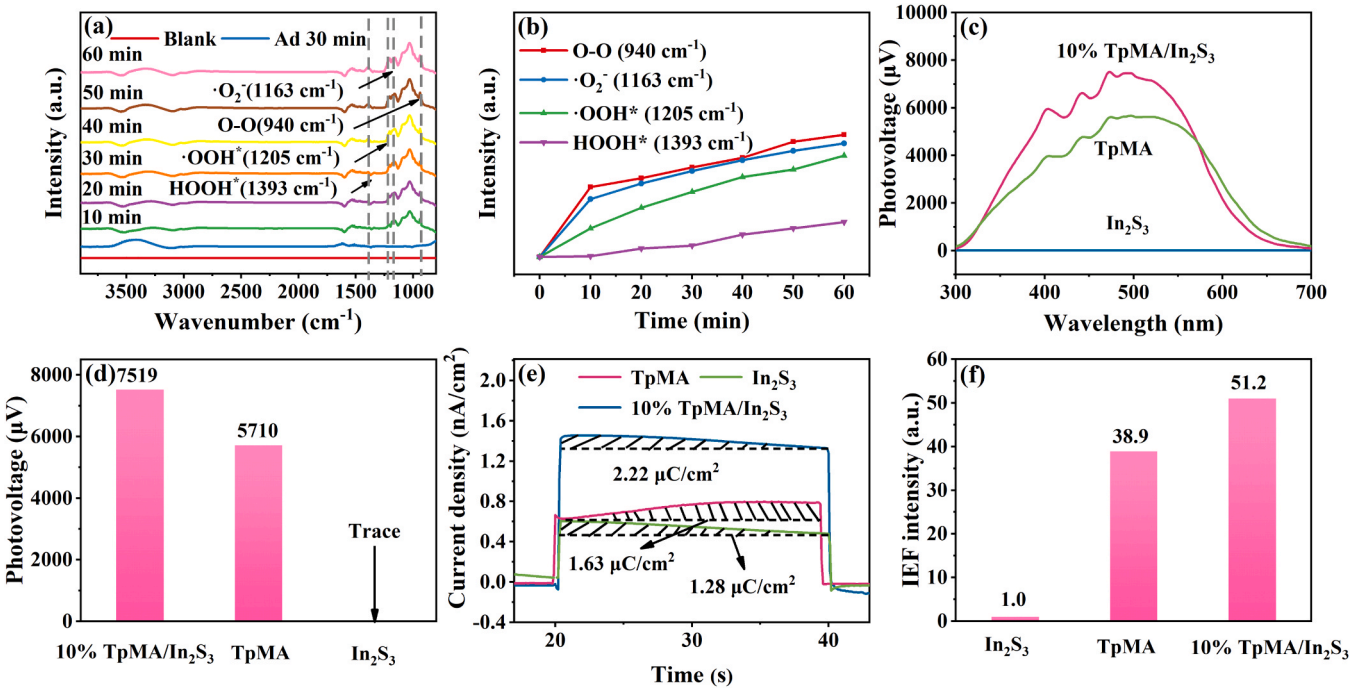

Fig. 3. The *in situ* FT-IR of 10%TpMA/In_2S_3 (a, b), the surface photovoltages of In_2S_3, TpMA and 10%TpMA/In_2S_3 (c, d), the charge density of In_2S_3, TpMA and 10% TpMA/In_2S_3 (e), and IEF of the In_2S_3, TpMA and 10%TpMA/In_2S_3 (f).

and 10%TpMA/In_2S_3. Using DMPO as a spin-trapping agent, DMPO-·O_2^- and DMPO-·OH were detected under irradiation (Fig. 4a and b). This analysis revealed that ·O_2^- constitutes a major active radical, and notably, no detectable ·OH species were observed in the reaction system. This observation aligns coherently with the position of CB and VB of the semiconductor within the photocatalyst. Notably, the 10%TpMA/In_2S_3 sample had the strongest DMPO-·O_2^- signal originating from O_2 reduction.

Based on the comprehensive analysis above, the H_2O_2 production of the 10%TpMA/In_2S_3 process can be delineated into two steps: (i): photo-induced electrons react with oxygen from air or water oxidation to produce ·O_2^-; (ii): ·O_2^- further react with photo-induced electrons to produce H_2O_2. The equation (Eqs. 2–7) can be depicted as follows:

$$2H_2O + 4h^+ \rightarrow O_2 + 4H^+ \quad (2)$$

$$O_2 + e^- \rightarrow \cdot O_2^- \quad (3)$$

$$\cdot O_2^- + H^+ \rightarrow \cdot OOH \quad (4)$$

$$\cdot OOH + \cdot OOH \rightarrow H_2O_2 + O_2 \quad (5)$$

$$\cdot OOH + \cdot O_2^- \rightarrow OOH^- + O_2 \quad (6)$$

$$OOH^- + H^+ \rightarrow H_2O_2 \quad (7)$$

The charge migration path of photogenerated electrons in the composite was comprehensively analyzed by an *in situ* XPS. As shown in Fig. 4c-f and S9, the C 1s, N 1s, S 2p, and In 3d spectra of the composite material 10%TpMA/In_2S_3 were obtained under light conditions. It was observed that the binding energies of C 1s and N 1s in 10%TpMA/In_2S_3 exhibited a noteworthy positive shift in comparison to their counterparts in the absence of light. Conversely, the binding energies of S 2p and In 3d in 10%TpMA/In_2S_3 showed a considerable negative shift. This spectral evidence supported the notion that photogenerated electrons in TpMA were transferred to In_2S_3 during illumination of 10%TpMA/In_2S_3. This observation provided compelling evidence for the presence of an S-scheme heterojunction, underscoring its significant role in enhancing the photocatalytic performance. To further comprehend the electron transport process, charge density difference was calculated employing DFT. The charge density difference of the TpMA/In_2S_3 heterojunction model was shown in Fig. 5a where blue and yellow regions symbolize electron consumption and accumulation, respectively.

This redistribution of charge yielded electron-rich areas on TpMA and electron-poor regions on In_2S_3, thus establishing a built-in electric field from In_2S_3 to TpMA. Furthermore, electron localization function (ELF) calculations disclosed electron concentration primarily around C and S atoms, along with an ELF value of approximately 0.5 electron gas encompassing all atoms, thereby indicating good conductivity (as evident in Fig. 5b). Strong interactions were observed between In and C elements, as reflected by ELF values ranging from 0.5 to 0.8, further substantiating the successful formation of heterojunction. Bader charge analysis revealed that C atoms in TpMA lost an average charge of 1.21, while N atoms lost an average charge of 1.24. In contrast, In_2S_3 exhibited an average charge of 1.26 for S atoms and 2.22 for In atoms (as evident in Fig. 5c). Notably, the positive charge values manifested strong electron attraction, particularly in the case of S and In atoms, indicative of Lewis acidity, thereby favoring in-plane charge transfer. Drawing upon the aforementioned analyses, the charge transfer process in 10% TpMA/In_2S_3 and its potential reaction mechanism were meticulously examined and elucidated. As shown in Fig. 5d-f, the difference in Fermi levels between In_2S_3 and TpMA prior to contact led to the transfer of electrons from In_2S_3 to TpMA upon contact until equilibrium of Fermi energy levels were achieved. This interfacial interaction prompted the establishment of an internal electric field from In_2S_3 to TpMA. Simultaneously, band bending occurred, with band bending upward for In_2S_3, and band bending downward for TpMA, respectively. Under visible light irradiation, this interplay between the internal electric field and band bending drove photo-generated electrons in the CB of TpMA to migrate across the interface and recombine with the holes in the VB of In_2S_3. This dynamic process facilitated efficient space charge separation, while

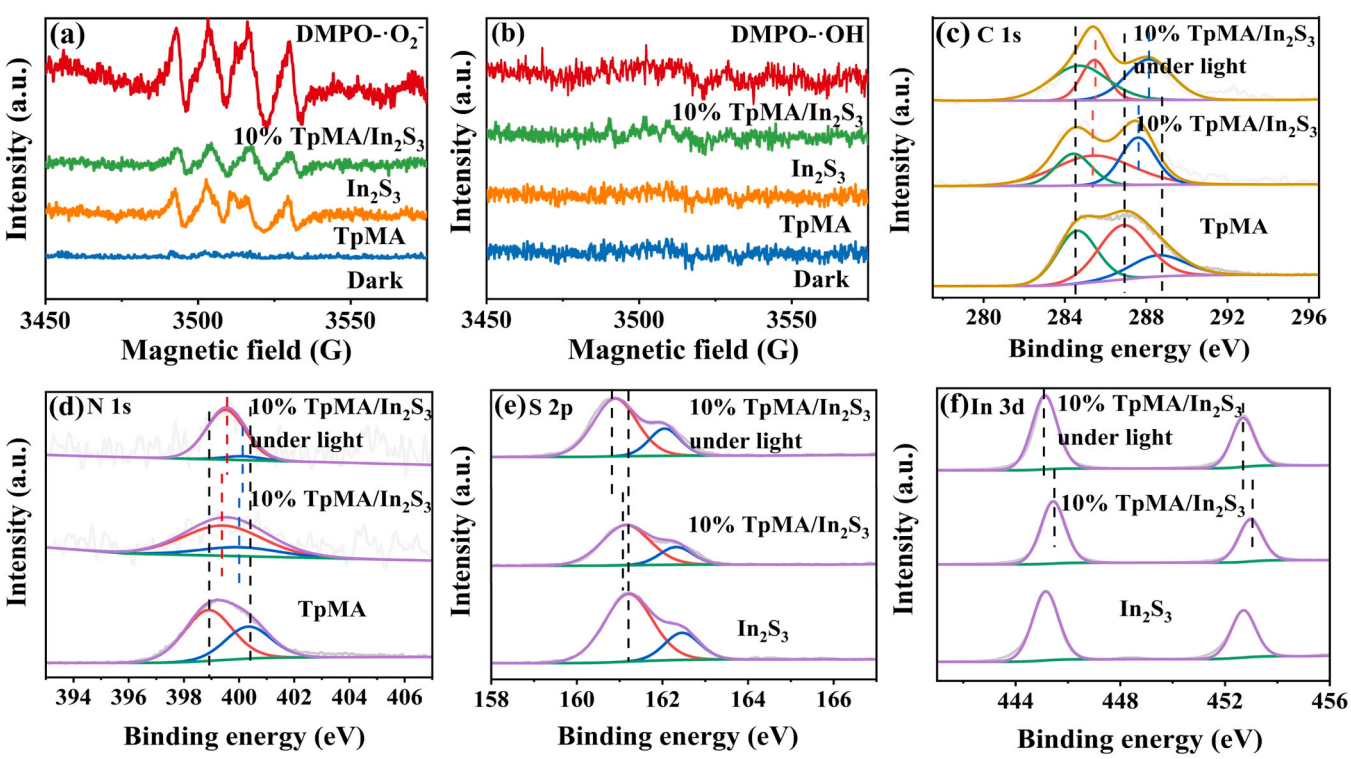

Fig. 4. EPR spectra of DMPO-·O_2^- in methanol dispersions of TpMA, In_2S_3 and 10%TpMA/In_2S_3 sample (a). EPR spectra of DMPO-·OH in aqueous dispersions of TpMA, In_2S_3 and 10%TpMA/In_2S_3 (b), *in situ* XPS spectra of 10%TpMA/In_2S_3 C 1s (c), N 1s (d), S 2p (e), In 3d (f).

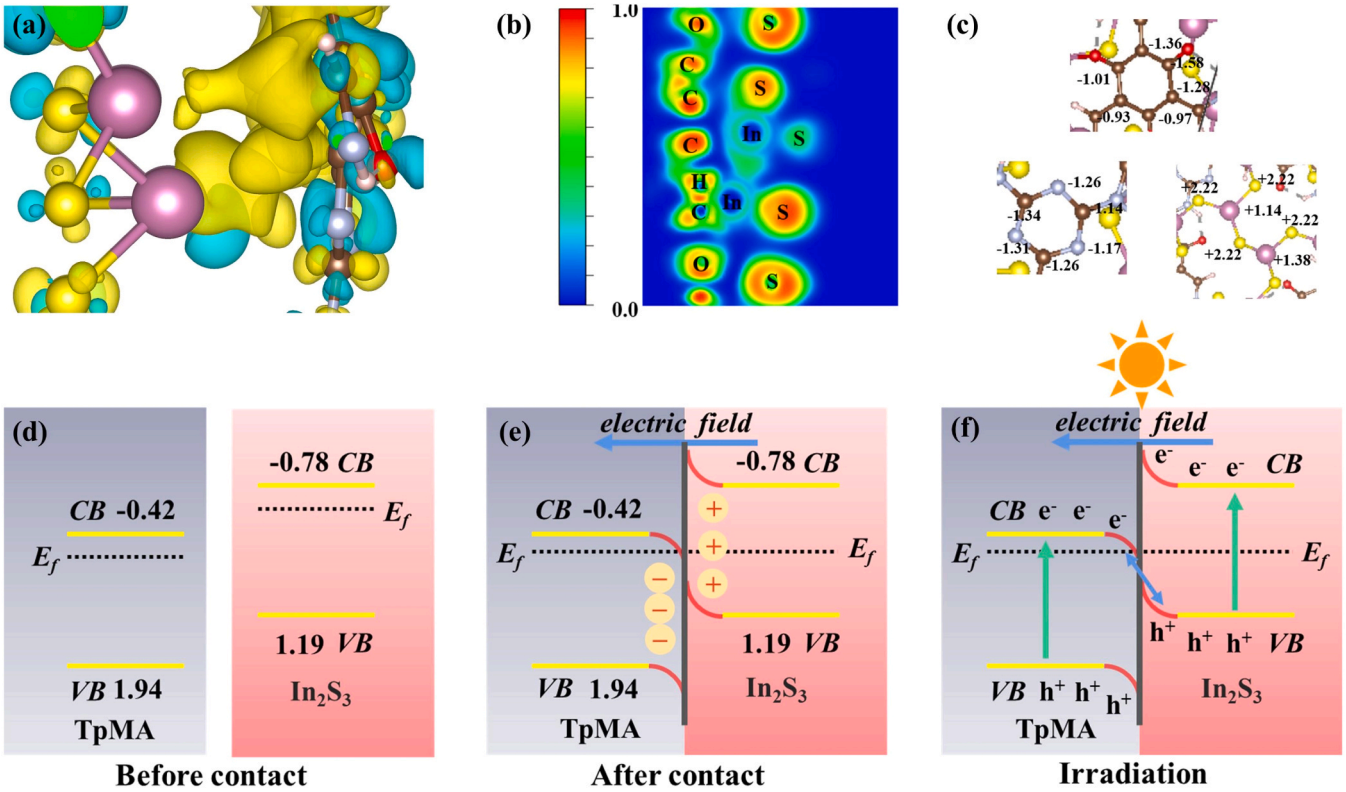

Fig. 5. The charge density difference (a), electron localization function (b) and bader of TpMA/In_2S_3 (c). Schematic illustration for photocatalytic H_2O_2 production of TpMA/In_2S_3 (d, e, f).

preserving the high potential reducing electrons in the CB of In_2S_3 and holes in the VB of TpMA. Consequently, the conventional S-scheme heterojunction mechanism aptly accounted for the amplified photocatalytic H_2O_2 production (Fig. 6).

3.6. Application in bacterial inactivation

Through constructing the *in situ* Fenton system, the H_2O_2 produced can be employed for various environmental applications, such as bacterial inactivation. When exposed to visible light, a series of photocatalysts demonstrated effective *E. coli* inactivation (Fig. 7a). It was clear that 10%TpMA/In_2S_3 and pure TpMA had moderate ability to inactivate *E. coli* within 150 min. The inactivation efficiency of *E. coli* was greatly improved by the addition of Fe(II). In the 10%TpMA/In_2S_3/Fe(II) system, complete inactivation of around 6.5 $\log_{10}$ cfu/mL cells could be accomplished in 150 min, but only 3.0 $\log_{10}$-reduction was demonstrated in 150 min in the TpMA/Fe(II) system. It demonstrated that adding Fe(II) activated the produced H_2O_2 on-site. As shown in Fig. 7b, the "Shoulder + log-linear + tail" model (Eq. 8) was used to fit the data and analyse the dynamic process of bacterial inactivation. ($R^2 = 0.98$ when plotting the relationship between log inactivation and time of killing *E. coli* with 10%TpMA/In_2S_3)

$$N(t) = \frac{N_0 * \exp(-K_{\max} * t) * (\exp(K_{\max} * S))}{(1 + (\exp(K_{\max} * S) - 1) * \exp(-K_{\max} * t))} \quad (8)$$

where N_0 and N(t) are the initial and survival number of cells (log, in cfu), respectively; K_{max} is the inactivation rate; and S is the shoulder length (min). Meanwhile, a homogenous Fenton system was built that can be utilized to render bacteria inactive. Using coumarin as the trapping agent, the yield of ·OH was quantified to show that hydrogen peroxide is activated *in situ* to ·OH. According to Fig. 7c, 7-hydroxycoumarin fluorescence intensity increased linearly with reaction time, indicating that ·OH was formed and caused the bacterial cell to inactivate. Without the addition of Fe(II), Fig. 7d demonstrated that the fluorescence intensity rose little. This outcome further showed that an *in situ* Fenton system could generate H_2O_2 that could be used directly to inactivate bacteria without the need for additional H_2O_2. Fig. 7e showed the coated plate variation of the bactericidal effect of 10%TpMA/In_2S_3 within 150 min. Considering that the bacteria subjected to disinfection treatment could have the potential to remain viable after disinfection and therefore leading to the bacterial regrowth phenomenon, the treated samples were tested for regrowth potential after dark storage for 12 h, 24 h, and 48 h. As shown in Table S2 and Fig. S10, no regrowth of *E. coli* was observed within 48 h. The results further confirmed the effectiveness of 10%TpMA/In_2S_3 in completely inactivating *E. coli* and the recontamination of bacterial regrowth can be avoided.

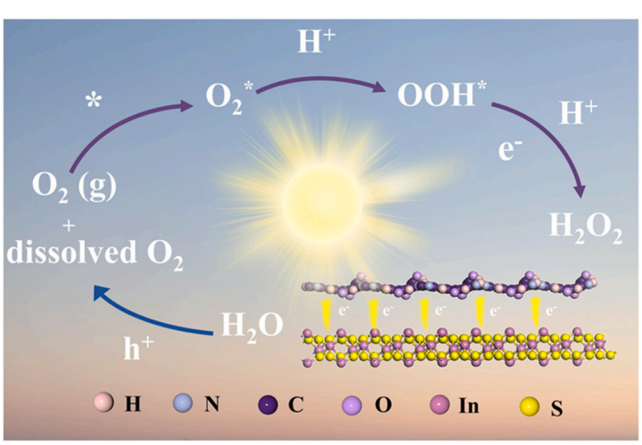

Fig. 6. Schematic illustration of photoproduction H_2O_2 by 10%TpMA/In_2S_3.

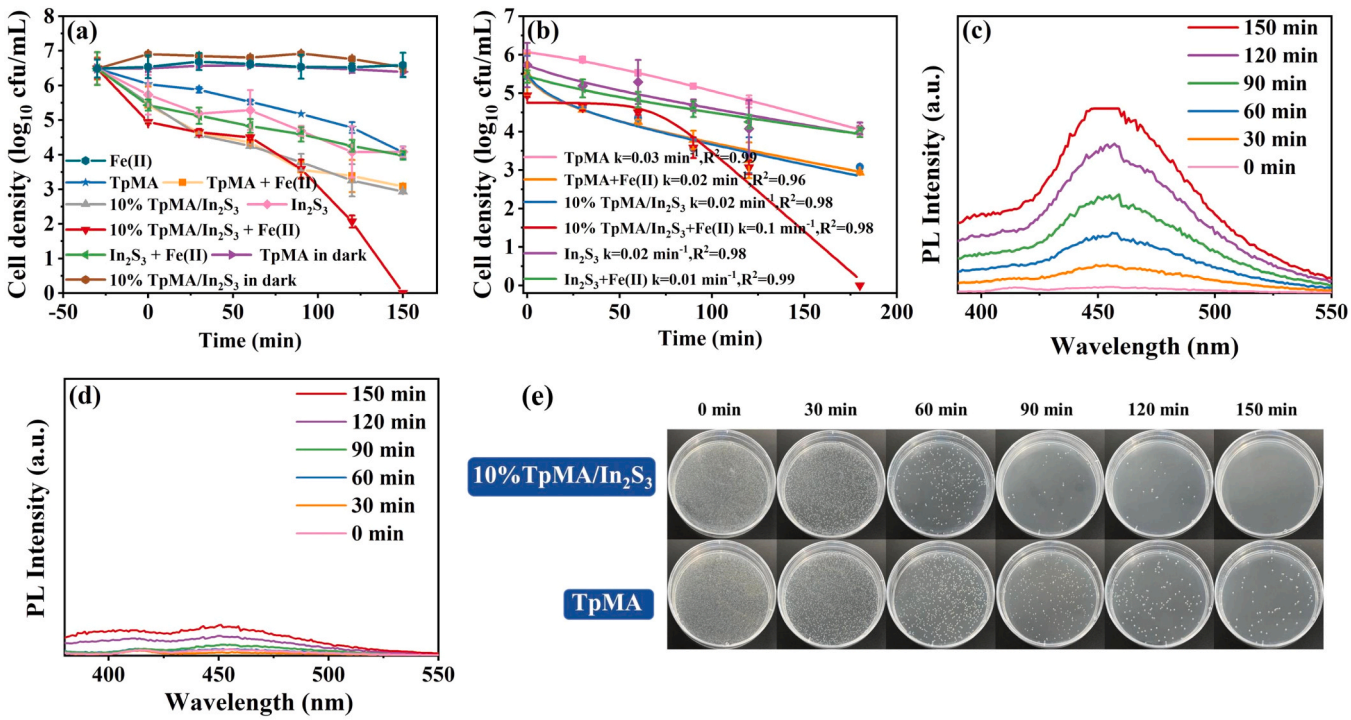

Fig. 7. Photocatalytic bacterial inactivation efficiency with and without Fe(II) (2.7 mM) addition (a). Photocatalytic inactivation kinetics of *E. coli* in the presence of 10%TpMA/In_2S_3 and Fe^{2+} under xenon lamp (b). Fluorescence spectra of coumarin solution (1 mM) in 10%TpMA/In_2S_3 with Fe(II) (c) and without Fe (II) under visible light irradiation (d). Effect diagram of the coated plate with bacterial solution sampled in different periods (above 10%TpMA/In_2S_3, below TpMA) (e).

4. Conclusions

In summary, a direct S-scheme TpMA/In_2S_3 composite photocatalyst was successfully synthesized via the hydrothermal method. Relative to TpMA, this S-scheme photocatalyst exhibited robust photoactivity for H_2O_2 generation, coupled with commendable reusability and quantum yield. The boosting photocatalytic activity could be ascribed to the ability of the S-scheme heterojunction to facilitate efficient carrier separation and migration, while simultaneously preserving strong reduction capability in In_2S_3 and potent oxidizability in TpMA. Furthermore, the generated H_2O_2, in the absence of exogenous H_2O_2, could be readily incorporated into an *in situ* Fenton system for bacterial inactivation in the presence of Fe(II) as a catalyst. Within 150 min of visible light exposure, complete inactivation of approximately 6.5 log_{10} cfu/mL *E. coli* cells was achieved. These findings underscore the potential of S-scheme heterojunction formation for H_2O_2 production in pure water and offer promising prospects for the development of external oxidant-free Fenton systems in diverse environmental control applications, including the inactivation of pathogenic microorganisms and the degradation of recalcitrant organic pollutants.

CRediT authorship contribution statement

Hanye Chen: Conceptualization, Experiment, Methodology, Investigation, Writing-original draft. **Shengjie Gao**: Formal analysis, Experiment, Data curation, Visualization. **Guocheng Huang**: Supervision, Formal analysis, Methodology, Data curation, Writing-review & editing. **Qiaoshan Chen**: Experiment, Investigation. **Yanxin Gao**: Formal analysis, Investigation. **Jinhong Bi:** Supervision, Formal analysis, Methodology, Data curation, Writing-review & editing.

Declaration of Competing Interest

The authors declare that they have no known competing financial interests or personal relationships that could have appeared to influence the work reported in this paper.

Data availability

Data will be made available on request.

Acknowledgments

This work was financially supported by the National Natural Science Foundation of China (22272028, 21707173), the Youth Talent Support Program of Fujian Province (00387077), the National Natural Science Foundation of Fujian Province (2022J01110).

Appendix A. Supporting information

Supplementary data associated with this article can be found in the online version at doi:10.1016/j.apcatb.2023.123545.

References

[1] F. Gosselin, L.M. Madeira, T. Juhna, J.C. Block, Drinking water and biofilm disinfection by Fenton-like reaction, Water Res. 47 (2013) 5631–5638.
[2] D.H. Kim, A.D. Bokare, M. Koo, W. Choi, Heterogeneous catalytic oxidation of As (III) on nonferrous metal oxides in the presence of H_2O_2, Environ. Sci. Technol. 49 (2015) 3506–3513.
[3] S. Zhang, H. Gao, Y. Huang, X. Wang, T. Hayat, J. Li, X. Xu, X. Wang, Ultrathin g-C_3N_4 nanosheets coupled with amorphous Cu-doped FeOOH nanoclusters as 2D/0D heterogeneous catalysts for water remediation, Environ. Sci. Nano 5 (2018) 1179–1190.
[4] J.K. Edwards, B. Solsona, E.N. N, A.F. Carley, A.A. Herzing, C.J. Kiely, G. J. Hutchings, Switching off hydrogen peroxide hydrogenation in the direct synthesis process, Science 323 (2009) 1037–1041.
[5] Z. Haider, H.-i Cho, G.-h Moon, H.-i Kim, Minireview: selective production of hydrogen peroxide as a clean oxidant over structurally tailored carbon nitride photocatalysts, Catal. Today 335 (2019) 55–64.
[6] C. Xia, Y. Xia, P. Zhu, L. Fan, H. Wang, Direct electrosynthesis of pure aqueous H_2O_2 solutions up to 20% by weight using a solid electrolyte, Science 366 (2019) 226–231.

[7] G.-h Moon, W. Kim, A.D. Bokare, N.-e Sung, W. Choi, Solar production of H_2O_2 on reduced graphene oxide-TiO_2 hybrid photocatalysts consisting of earth-abundant elements only, Energy Environ. Sci. 7 (2014) 4023–4028.

[8] J. Rodríguez-Chueca, M.P. Ormad, R. Mosteo, S. Canalis, J.L. Ovelleiro, Escherichia colilnactivation in fresh water through photocatalysis with TiO_2-effect of H_2O_2 on disinfection kinetics, Clean Soil Air Water 44 (2016) 515–524.

[9] R. Arrigo, M.E. Schuster, S. Abate, G. Giorgianni, G. Centi, S. Perathoner, S. Wrabetz, V. Pfeifer, M. Antonietti, R. Schlögl, Pd supported on carbon nitride boosts the direct hydrogen peroxide synthesis, ACS Catal. 6 (2016) 6959–6966.

[10] S. Shibata, T. Suenobu, S. Fukuzumi, Direct synthesis of hydrogen peroxide from hydrogen and oxygen by using a water-soluble iridium complex and flavin mononucleotide, Angew. Chem. Int. Ed. 52 (2013) 12327–12331.

[11] M. Kou, Y. Wang, Y. Xu, L. Ye, Y. Huang, B. Jia, H. Li, J. Ren, Y. Deng, J. Chen, Y. Zhou, K. Lei, L. Wang, W. Liu, H. Huang, T. Ma, Molecularly engineered covalent organic frameworks for hydrogen peroxide photosynthesis, Angew. Chem. Int. Ed. 61 (2022), e202200413.

[12] X. Chen, Y. Kuwahara, K. Mori, C. Louis, H. Yamashita, A hydrophobic titanium doped zirconium-based metal organic framework for photocatalytic hydrogen peroxide production in a two-phase system, J. Mater. Chem. A 8 (2020) 1904–1910.

[13] S. Hu, X. Qu, P. Li, F. Wang, Q. Li, L. Song, Y. Zhao, X. Kang, Photocatalytic oxygen reduction to hydrogen peroxide over copper doped graphitic carbon nitride hollow microsphere: the effect of Cu(I)-N active sites, Chem. Eng. J. 334 (2018) 410–418.

[14] Y. Qin, G. Dong, L. Zhang, G. Li, T. An, Highly efficient and selective photoreduction of CO_2 to CO with nanosheet g-C_3N_4 as compared with its bulk counterpart, Environ. Res. 195 (2021), 110880.

[15] J. Lai, X. Jiang, M. Zhao, S. Cui, J. Yang, Y. Li, Thickness-dependent layered $BiOIO_3$ modified with carbon quantum dots for photodegradation of bisphenol A: mechanism, pathways and DFT calculation, Appl. Catal. B Environ. 298 (2021), 120622.

[16] M.G. Schwab, M. Hamburger, X. Feng, J. Shu, H.W. Spiess, X. Wang, M. Antonietti, K. Mullen, Photocatalytic hydrogen evolution through fully conjugated poly (azomethine) networks, Chem. Commun. 46 (2010) 8932–8934.

[17] C.E. Chan-Thaw, A. Villa, L. Prati, A. Thomas, Triazine-based polymers as nanostructured supports for the liquid-phase oxidation of alcohols, Chem. Eur. J. 17 (2011) 1052–1057.

[18] C. Krishnaraj, H. Sekhar Jena, L. Bourda, A. Laemont, P. Pachfule, J. Roeser, C. V. Chandran, S. Borgmans, S.M.J. Rogge, K. Leus, C.V. Stevens, J.A. Martens, V. Van Speybroeck, E. Breynaert, A. Thomas, P. Van Der Voort, Strongly reducing (Diarylamino)benzene-based covalent organic framework for metal-free visible light photocatalytic H_2O_2 generation, J. Am. Chem. Soc. 142 (2020) 20107–20116.

[19] G. Zhao, S.A. Bonke, S. Schmidt, Z. Wang, B. Hu, T. Falk, Y. Hu, T. Rath, W. Xia, B. Peng, A. Schnegg, Y. Weng, M. Muhler, Highly efficient and selective aerobic oxidation of cinnamyl alcohol under visible light over Pt-loaded $NaNbO_3$ enriched with oxygen vacancies by Ni doping, ACS Sustain. Chem. Eng. 9 (2021) 5422–5429.

[20] B. Gao, X. Yu, T. Wang, H. Gong, X. Fan, H. Xue, C. Jiang, K. Chang, X. Huang, J. He, Promoting charge separation by rational integration of a covalent organic framework on a $BiVO_4$ photoanode, Chem. Commun. 58 (2022) 1796–1799.

[21] Y. Huang, P. Du, W.-X. Shi, Y. Wang, S. Yao, Z.-M. Zhang, T.-B. Lu, X. Lu, Filling COFs with bimetallic nanoclusters for CO_2-to-alcohols conversion with H_2O oxidation, Appl. Catal. B Environ. 288 (2021), 120001.

[22] S.S. Zhao, J. Liang, D.-H. Si, M.-J. Mao, Y.B. Huang, R. Cao, Superheterojunction covalent organic frameworks: supramolecular synergetic charge transfer for highly efficient photocatalytic CO_2 reduction, Appl. Catal. B Environ. 333 (2023), 122782.

[23] C.-C. Li, M.-Y. Gao, X.-J. Sun, H.-L. Tang, H. Dong, F.-M. Zhang, Rational combination of covalent-organic framework and nano TiO_2 by covalent bonds to realize dramatically enhanced photocatalytic activity, Appl. Catal. B Environ. 266 (2020), 118586.

[24] J. Wang, Y. Yu, J. Cui, X. Li, Y. Zhang, C. Wang, X. Yu, J. Ye, Defective g-C_3N_4/covalent organic framework van der waals heterojunction toward highly efficient S-scheme CO_2 photoreduction, Appl. Catal. B Environ. 301 (2022), 120814.

[25] Y. Wang, Z. Hu, W. Wang, H. He, L. Deng, Y. Zhang, J. Huang, N. Zhao, G. Yu, Y. N. Liu, Design of well-defined shell-core covalent organic frameworks/metal sulfide as an efficient Z-scheme heterojunction for photocatalytic water splitting, Chem. Sci. 12 (2021) 16065–16073.

[26] D. Xia, W. Wang, R. Yin, Z. Jiang, T. An, G. Li, H. Zhao, P.K. Wong, Enhanced photocatalytic inactivation of Escherichia coli by a novel Z-scheme g-C_3N_4 /m-Bi_2O_4 hybrid photocatalyst under visible light: the role of reactive oxygen species, Appl. Catal. B Environ. 214 (2017) 23–33.

[27] L. Zhang, J. Zhang, H. Yu, J. Yu, Emerging S-scheme photocatalyst, Adv. Mater. 34 (2022) 2107668.

[28] F. Xu, K. Meng, B. Cheng, S. Wang, J. Xu, J. Yu, Unique S-scheme heterojunctions in self-assembled TiO_2/$CsPbBr_3$ hybrids for CO_2 photoreduction, Nat. Commun. 11 (2020) 4613.

[29] M. Murugalakshmi, G. Mamba, S.A. Ansari, V. Muthuraj, T.I.T. Nkambule, Ultrasonic assisted anchoring of Yb_2O_3 nanorods on In_2S_3 nanoflowers for norfloxacin degradation and Cr(VI) reduction in water: kinetics and degradation pathway, Colloid Surf. A 634 (2022), 127969.

[30] K. Zhang, M. Zhou, K. Yang, C. Yu, P. Mu, Z. Yu, K. Lu, W. Huang, W. Dai, Photocatalytic H_2O_2 production and removal of Cr (VI) via a novel Lu_3NbO_7: Yb, Ho/CQDs/$AgInS_2$/In_2S_3 heterostructure with broad spectral response, J. Hazard. Mater. 423 (2022), 127172.

[31] H. Qiu, S. Fang, G. Huang, J. Bi, A novel application of In_2S_3 for visible-light-driven photocatalytic inactivation of bacteria: kinetics, stability, toxicity and mechanism, Environ. Res 190 (2020), 110018.

[32] W. Wang, G. Li, D. Xia, T. An, H. Zhao, P.K. Wong, Photocatalytic nanomaterials for solar-driven bacterial inactivation: recent progress and challenges, Environ. Sci. Nano 4 (2017) 782–799.

[33] Y. Li, P. Han, Y. Hou, S. Peng, X. Kuang, Oriented $ZnmIn_2S_{m+3}$@In_2S_3 heterojunction with hierarchical structure for efficient photocatalytic hydrogen evolution, Appl. Catal. B Environ. 244 (2019) 604–611.

[34] Y. Li, Y. Hou, Q. Fu, S. Peng, Y.H. Hu, Oriented growth of $ZnIn_2S_4$/$In(OH)_3$ heterojunction by a facile hydrothermal transformation for efficient photocatalytic H_2 production, Appl. Catal. B Environ. 206 (2017) 726–733.

[35] M.J. Bojdys, J. Jeromenok, A. Thomas, M. Antonietti, Rational extension of the family of layered, covalent, triazine-based frameworks with regular porosity, Adv. Mater. 22 (2010) 2202–2205.

[36] P. Kuhn, M. Antonietti, A. Thomas, Porous, Covalent triazine-based frameworks prepared by ionothermal synthesis, Angew. Chem. Int. Ed. 47 (2008) 3450–3453.

[37] S. He, Q. Rong, H. Niu, Y. Cai, Construction of a superior visible-light-driven photocatalyst based on a C_3N_4 active centre-photoelectron shift platform-electron withdrawing unit triadic structure covalent organic framework, Chem. Commun. 53 (2017) 9636–9639.

[38] Z. Zou, X. Wang, J. Huang, Z. Wu, F. Gao, An Fe-doped nickel selenide nanorod/nanosheet hierarchical array for efficient overall water splitting, J. Mater. Chem. A 7 (2019) 2233–2241.

[39] B. Chai, T. Peng, J. Mao, K. Li, L. Zan, Graphitic carbon nitride (g-C_3N_4)-Pt-TiO_2 nanocomposite as an efficient photocatalyst for hydrogen production under visible light irradiation, Phys. Chem. Chem. Phys. 14 (2012) 16745–16752.

[40] E. Karamian, S. Sharifnia, On the general mechanism of photocatalytic reduction of CO_2, J. CO_2 Util. 16 (2016) 194–203.

[41] T. Kanata-Kito, M. Matsunaga, H. Takakura, Y. Hamakawa, T. Nishino, Photoreflectance characterization of built-in potential in MBE-produced as-grown GaAs surface, Proc. SPIE 56 (1990) 1286.

[42] X. Chen, J. Wang, Y. Chai, Z. Zhang, Y. Zhu, Efficient photocatalytic overall water splitting induced by the giant internal electric field of a g-C_3N_4/rGO/PDIP Z-Scheme heterojunction, Adv. Mater. 33 (2021) 2007479.